Evaluation of Budget Analyses during MISMO

MASAKI KATSUMATA

Research Institute for Global Change, Japan Agency for Marine–Earth Science and Technology, Yokosuka, Japan, and Department of Atmospheric Science, Colorado State University, Fort Collins, Colorado

PAUL E. CIESIELSKI AND RICHARD H. JOHNSON

Department of Atmospheric Science, Colorado State University, Fort Collins, Colorado

(Manuscript received 19 March 2010, in final form 13 August 2010)

ABSTRACT

Results of sounding-derived heat and moisture budgets for the *Mirai* Indian Ocean Cruise for the Study of the MJO Onset (MISMO) project in 2006 are evaluated using observational and simulated datasets. Estimated rainfall rates from the budget analyses agree well with both the satellite-derived products and in situ rain gauge measurements in the period leading up to the convectively active phase of the MJO. During the active phase, however, large discrepancies are found in the temporal variation of the rainfall estimates on the time scale of a few to several days. Utilizing MJO circulations simulated by the two numerical models, a linear model and a high-resolution AGCM, it is revealed that this discrepancy may result from inability of the MISMO triangular network to properly capture the divergence associated with the Rossby and/or inertia–gravity wave components of the circulation. A rectangular array is demonstrated to be superior at capturing the wind associated with these wave disturbances. Possible effects of the equatorial waves and sampling issues, which could act to enhance or suppress the error in the present case, are discussed. The reliability of the budget analyses during the preactive period is also supported by both model simulations.

1. Introduction

Diabatic heating by convective systems is one of the important driving forces of the atmospheric circulation. Diabatic heating impacts both the global atmospheric circulation (e.g., Hartmann et al. 1984; Schumacher et al. 2004) and the local circulation (e.g., Nicholls et al. 1991; Mapes and Houze 1995; Lin et al. 2004) by exciting a variety of wave types.

To observationally estimate diabatic heating and moistening by convective systems, budget analysis of heat and moisture using upper-air soundings (or ''budget analysis'') is traditionally utilized, especially by the method of Yanai et al. (1973). Their method is to calculate the apparent heat source Q_1 and apparent moisture sink Q_2 by adding the horizontal and vertical advective components to the observed temporal variation of dry static energy (for Q_1) and water vapor mixing ratio (for Q_2).

The accuracy of this widely used approach, however, is affected by various factors, including the temporal and spatial sampling of the sounding array (e.g., Mapes et al. 2003), as well as the configuration of the network (e.g., Ciesielski et al. 1999). Therefore, evaluating the reliability of the budget analyses is useful when these estimated values are utilized in further analyses. For example, in the case of the Tropical Ocean and Global Atmosphere Coupled Ocean–Atmosphere Response Experiment (TOGA COARE), Johnson and Ciesielski (2000) and Ciesielski et al. (2003) evaluated the reliability of the budget analyses by comparing budget-derived rainfall estimates to those from independent sources.

Recently, the *Mirai* Indian Ocean Cruise for the Study of the MJO Onset (MISMO; see Yoneyama et al. 2008b, hereinafter Y08) conducted special sounding observations to enable budget analyses over the tropical Indian Ocean. Katsumata et al. (2009, hereinafter KJC09) utilized the budget analyses to investigate the synoptic-scale eastward-propagating disturbances in MISMO, which appeared to be convectively coupled Kelvin waves. Unfortunately, the

---

Corresponding author address: Masaki Katsumata, Research Institute for Global Change, Japan Agency for Marine-Earth Science and Technology (JAMSTEC), Natsushima-cho 2-15, Yokosuka 237-0061, Japan.
E-mail: katsu@jamstec.go.jp

DOI: 10.1175/2010JAMC2515.1

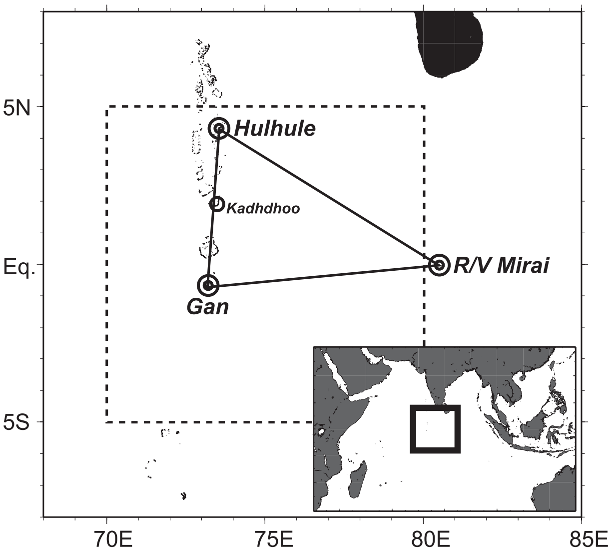

FIG. 1. Map of MISMO domain showing the observation sites used in this study. Inset map in lower-right-hand corner shows the location and domain of the enlarged map. The double circles indicate upper-air sounding sites with rain gauge, while the single circle indicates a rain gauge site without upper-air observations. The broken rectangle is a 10° × 10° box used in Fig. 5 to obtain averaged divergence derived by QuikSCAT data.

sounding network in MISMO was not comparable to that in TOGA COARE and other field campaigns [e.g., Global Atmospheric Research Program (GARP) Atlantic Tropical Experiment (GATE); the South China Sea Monsoon Experiment (SCSMEX)] in terms of spatial density of soundings and their launch frequency (see section 2 for detail). As pointed out by Zhang et al. (2001) and Mapes et al. (2003), the spatial and temporal sampling directly affects the accuracy of the budget analyses. As a result, the poorer sampling in MISMO would potentially lead to larger budget errors than in TOGA COARE. Furthermore, Ciesielski et al. (1999) reported that the triangle configuration of a sounding array may result in significant errors in estimated divergence related to undersampling of the rotational wind. Because the MISMO sounding network utilized only three sounding sites (Fig. 1), and the rotational wind component is large in certain equatorial waves, such effects should be also examined in the MISMO sounding array.

This study aims to determine the reliability of the budget analyses during MISMO, and investigates the factors that affect their reliability. In section 2, the sounding network and budget method are introduced. The results of the budget analyses are evaluated in section 3 by comparing budget-estimated rainfall rates to those from other observational sources, as in Johnson and Ciesielski (2000). The following sections examine the reasons for the observed rainfall differences by using observational data and two numerical simulations. One of the simulations is from a linear model that computes the idealized response to an MJO-like heat source (section 4), and the other is from a high-resolution AGCM that reproduced the intraseasonal oscillation observed during MISMO (section 5). The results of the simulations are then compared with the observed MISMO case in section 6 to identify the causes of the budget errors. Section 7 summarizes the results and discussions.

2. Budget analyses

Within the MISMO observation period, three soundings at the research vessel (R/V) *Mirai* (0°, 80.5°E), Gan Island (0.7°S, 73.2°E), and Hulhule (4.2°N, 73.5°E) (see Fig. 1 for locations) were available from 31 October to 26 November 2006 [also known as arrayed sounding period (ASP) as in KJC09]. In the ASP, the sonde launch frequency varied among these sites; every 3 h throughout the ASP at the R/V *Mirai*, every 12 h prior to 13 November and every 6 h thereafter at Gan, and every 12 h prior to 20 November and every 6 h thereafter at Hulhule. See Y08 for additional details of the observations.

This study utilizes all sounding datasets obtained during the ASP. When necessary, sounding data were interpolated in time to facilitate a 6-h analysis frequency throughout the ASP at all sites. A daytime dry bias in the Vaisala RS92 humidity sensors is corrected as in Yoneyama et al. (2008a) for all individual soundings.

The budget analysis method to obtain Q_1 and Q_2 in the present study is the same as in KJC09 based on Yanai et al. (1973). First, the gridded fields of wind, temperature, and water vapor mixing ratio were created at 6 h, 1° horizontal, 25-hPa vertical resolution using multiquadric interpolation (Nuss and Titley 1994). These gridded fields were then used to diagnose divergence, mass-balanced vertical motion (using the method of O'Brien 1970), and to compute Q_1 and Q_2. Since the disturbance studied in Y08 and KJC09 was an abortive MJO, it will be hereinafter referred to by the more general term intraseasonal oscillation (ISO).

Figure 2 shows the ASP-averaged vertical profile of Q_1 and Q_2, along with the profiles from TOGA COARE (Johnson and Ciesielski 2000), which captured the convectively active phases of MJO in the western Pacific. The Q_1 profiles from these two experiments bear a strong resemblance to each other, with peak heating values about 4 K day^{-1} near 400 hPa in both cases. Above 600-hPa height, the Q_2 profiles from these two regions also show a strong resemblance. Similar characteristics in Q_1 and Q_2 were observed in the SCSMEX Northern Enhanced Sounding Array (NESA) (Johnson and Ciesielski 2002), which captured deep convection during and after the onset of the Asian summer monsoon. Even in the Kwajalein Experiment (KWAJEX), Schumacher et al. (2008) observed profiles with similar characteristics during periods

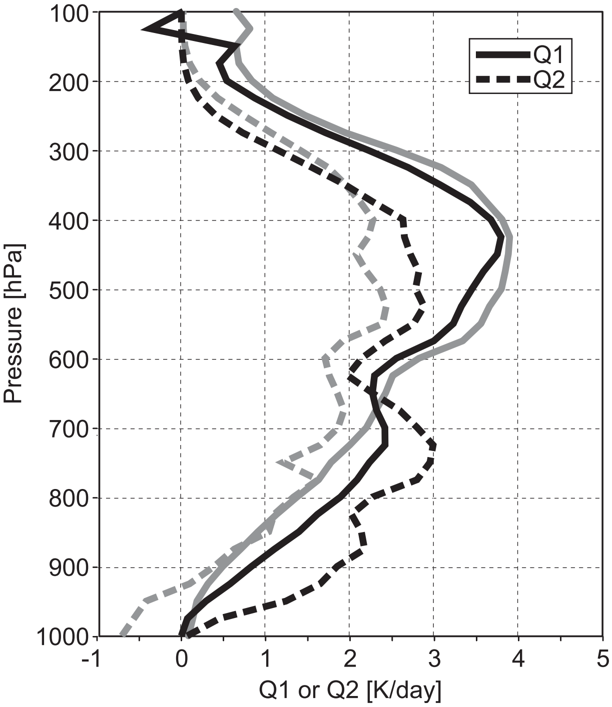

FIG. 2. Period-averaged vertical profile of Q_1 and Q_2, for MISMO-ASP (black) and TOGA COARE intensive observing period (IOP) (gray).

of convectively disturbed weather. These similarities to other experiments suggest that the MISMO-ASP-mean profiles in Fig. 2 are consistent with periods of deep convection as observed during the latter portions of the ASP (see Y08 and KJC09).

On the other hand, the MISMO Q_1 and Q_2 mean values were slightly larger in the layer below 600-hPa height than those observed in TOGA COARE. Such characteristics corroborate the findings of KJC09, which showed that abundant shallow convection and corresponding shallow heating were present before the convectively active period. The bimodal Q_2 pattern with the layer of $Q_1 < Q_2$ below 650-hPa height resembles the profiles in Yanai et al. (1973) for Marshall Islands, in which both deep and shallow convection were frequently observed. Zhang and Hagos (2009) demonstrated that the bimodal structure of the diabatic heating is a common feature in the eight field experiments, including MISMO, which they examined. These characteristics and their similarities to previous experiments suggest that the ASP-averaged profiles for MISMO, which include both convectively active and inactive periods, are reasonable.

3. Comparison of estimated rainfall amounts

To evaluate the consistency of the computed Q_1 and Q_2, the estimated rainfall amount from the budget analyses is compared with observed rainfall from other independent sources. The estimated rainfall from the budget analyses is calculated as in Yanai et al. (1973) from $\langle Q_2 \rangle = L(P - E)$, where L is the latent heat of vaporization, P is precipitation rate, E is surface evaporation rate, and $\langle\ \rangle$ represents the vertical integral over the depth of the troposphere. The latent heat flux from the sea surface (E) is obtained from the Woods Hole Oceanographic Institution objectively analyzed air–sea fluxes (WHOI OAFlux) dataset (Yu et al. 2008), which is at 1° horizontal resolution. As in KJC09, these values are adjusted by the ratio of the ASP-averaged observed eddy fluxes at the R/V *Mirai* (Takahashi et al. 2005) to the ASP-averaged OAFluxes at the grid point closest to the R/V *Mirai*. The adjustment ratio was 0.80.

For the comparison, we prepare three other datasets of rainfall amount. Two of them are from satellites, and another is from the surface rain gauges. In situ rain gauges were installed and provided continuous rainfall data at four points on the edges of budget analysis area: R/V *Mirai*, Gan Island, Hulhule Island, and Kadhdhoo Island (1.9°N, 73.5°E) (see Fig. 1 for their locations). Tipping-bucket rain gauges were used on the island sites to provide measurements of rainfall amount every 10 min. A capacitance rain gauge was operated on the R/V *Mirai* to provide rainfall amount every 1 min. These rainfall data were converted to 6-hourly data for each site, then averaged together to utilize as domain-averaged value. An advantage of the surface rain gauge data is their full coverage of the temporal variation. The limited spatial sampling, especially lack of observations within the sounding array, is a disadvantage.

Two satellite estimates of rainfall are used. One is Special Sensor Microwave Imager (SSM/I)-derived rainfall estimates (Wentz and Spencer 1998), while the other is the Global Satellite Map for Precipitation (GSMaP; Kubota et al. 2007). The former is derived from microwave radiometer measurements only. The latter is a combined product using both microwave and infrared radiometers. The satellite estimates have the advantage of broad areal coverage. The limited number of overpasses of the microwave radiometers (a few to several times in a day) is their disadvantage, though the GSMaP product fills the temporal gaps by using hourly infrared images.

The analysis period, that is, MISMO-ASP, covered the transition period from a convectively inactive period to an active period, as described in Y08 and KJC09. Thus, the ASP contained a wide variety of precipitating clouds and disturbances, ranging from shallow cumulus to organized deep convection.

The measured and estimated rainfall rates from the methods described above for the 26-day ASP are shown in Table 1. The estimate of the ASP-mean rain rate from the budget analysis differs by about 10% or less from the

TABLE 1. Observed and estimated rainfall amount averaged for the MISMO-ASP.

Method	Rainfall (mm day^{-1})			Correlation coef with budget analysis	
	ASP	Preactive	Active	Preactive	Active
Budget analysis	9.9	6.3	15.0	—	—
Rain gauges	11.1	7.9	15.3	0.76	0.26
GSMaP	10.7	6.5	16.5	0.82	0.22
SSM/I	10.6	7.9	14.6	0.79	0.38

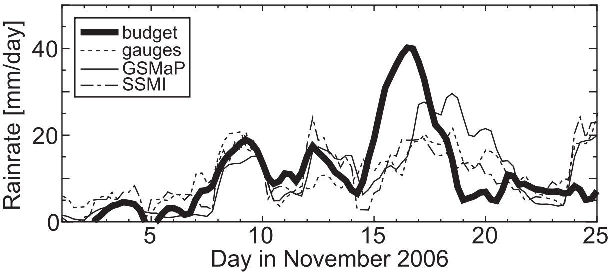

FIG. 3. Time series of observed and estimated rainfall during MISMO-ASP. A 2-day running mean is applied to all data.

other estimates. This difference is similar to that found by Johnson and Ciesielski (2000) in the 4-month mean TOGA COARE rain rate between budget-derived estimates and those from other independent sources (satellite products, rain gauges, and shipborne radars). Considering that the TOGA COARE budget analyses utilized a denser sounding network for a much longer period (i.e., 4 months), the differences in the present study for MISMO can be considered reasonably small.

Time series of the various rainfall estimates are shown in Fig. 3. All values in the figure are averaged temporally, applying a 2-day running mean to remove the effect of diurnal and short-term variability on the different temporal samplings. In the period leading up to the convectively active phase of the ISO (i.e., prior to 15 November, KJC09, or preactive period), there is good agreement among the various estimates. For this preactive period, the averaged rainfall rates based on the different estimates agree reasonably well, as shown in Table 1. The correlation coefficients between budget-estimate and other measurements, also in Table 1, are statistically significant at the 99% level for the preactive period. These findings indicate that the budget analyses yield reasonable results in the preactive period.

During the convectively active phase (or active period) after 15 November, the period-averaged rainfall amounts in Table 1 also match well to each other. However, the correlations between the budget analyses and other estimates drastically drop from the high values in the preactive phase. The detailed time series of the estimated rainfalls (Fig. 3) show the large discrepancies in the six days from 15 November, when the convectively active phase began and largest rainfall event was captured by all estimates. The budget analyses indicate maximum rainfall on 16 November, with peak values nearly double those observed in the preactive period, followed by the rapid drop to the minimum after 19 November. Meanwhile, the other estimates (gauges and satellites) indicate moderate rainfall amounts (i.e., slightly larger than the peaks in the preactive period) around 16–18 November without any rapid drop. Considering that the other estimates (gauges and satellites) are significantly correlated to each other (not shown), only the budget analysis is an outlier in its temporal variation (Fig. 3) for these six days.

These results suggest that in the active period, variations on the time scale of a few to several days are not captured correctly by the budget analyses, though the period average appears reasonable. Considering that the ASP-averaged surface latent heat flux contributed to the rainfall about 2.4 mm day^{-1} with a standard deviation of 0.4 mm day^{-1}, the discrepancy of the estimated rainfall by the budget analyses is due to the estimation of $\langle Q_2 \rangle$.

4. Simulation using linear model

The temporal change in the accuracy of the budget analyses, shown in the previous section, suggests that the discrepancy in the active period is not caused by simple random sampling issues (Mapes et al. 2003), which theoretically give rise to errors regardless of the temporal evolution of the phenomenon. Thus, other possible causes are examined here.

One possibility for the large discrepancies between the budget analyses and the other estimates during the active phase could be related to the triangular configuration of the MISMO sounding network and the large station spacing. For example, Ciesielski et al. (1999) showed that the triangular configuration of the Atlantic Stratocumulus Transition Experiment (ASTEX) sounding array could result in a 20% error in divergence associated with the passage of an idealized Rossby wave. The results of the budget analyses (especially in the tropics where horizontal advection is small) depend largely on the estimated vertical motion, and this field, in turn, by divergence.

The present study considers an analysis similar to Ciesielski et al. (1999) to investigate the possible cause of the large discrepancy in the convectively active phase shown in the previous section. Since the active period during MISMO had the formative characteristics of an MJO (Y08; KJC09), a simulated wind field is produced by forcing a linearized, equatorial β-plane primitive equation model (Schubert and Masarik 2006) with an MJO-like

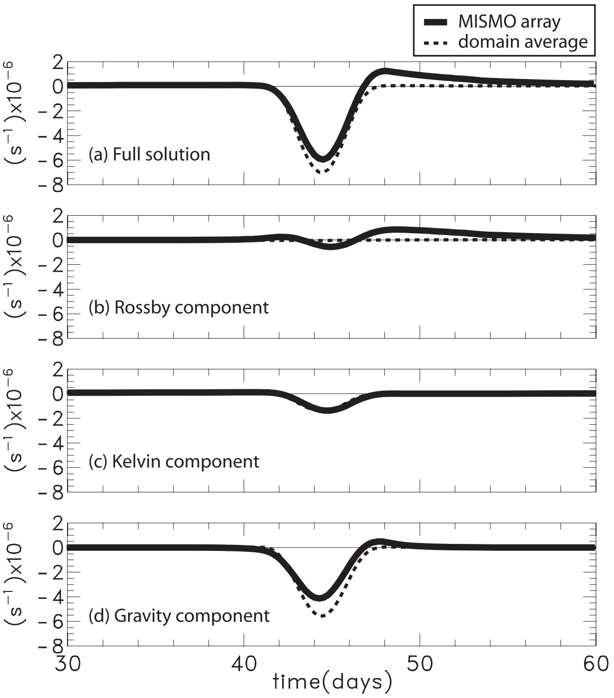

FIG. 4. Time series of the divergence at 850-hPa height within the MISMO sounding array (triangular area in Fig. 1), calculated from the theoretical wind field of Schubert and Masarik (2006). The broken line indicates the simple areal average within the triangular area, while the solid line is from the reconstructed wind sampled at the three MISMO sounding sites (see text for details). The four panels are for (a) total solution, (b) Rossby component, (c) Kelvin wave component, and (d) inertia–gravity wave component as in Fig. 3 of Schubert and Masarik (2006).

convective heat source. Because the period-averaged MISMO Q_1 profile closely resembles that from TOGA COARE (Fig. 2), the present study also adopts the same vertical heating structure as in the original, which is based on the TOGA COARE Q_1 profile during an MJO passage with a peak magnitude of 12.5 K day^{-1}. The zonal half-width of the heating was specified as 1250 km, and an *e*-folding width in *y* direction (meridional direction) of 450 km. These parameters are the same as in Schubert and Masarik (2006). The eastward movement of the convectively active packet is simulated by moving the heat source eastward with a speed of 5 m s^{-1}, similar to the observed speed (Fig. 5 of Y08). In addition, the design of the model allows one to separate contributions to the wind field from the various wave mode components (i.e., Kelvin, Rossby, inertia–gravity, etc.).

Figure 4 shows the divergence time series at 850 hPa computed using high spatial resolution (~10 km) model winds to compute divergence then averaging it over the MISMO domain (dotted line), and secondly, by sampling the model winds at the three MISMO sounding points, objectively analyzing them onto a 1° grid, computing divergence on this grid, then averaging divergence over the MISMO domain (solid line).[1] The result shows that using only the three MISMO points results in an erroneous divergence, especially after the passage of the heat source. Figures 4b–d indicate that this false divergence appears mainly in the Rossby wave and inertia–gravity wave components, while the divergence from Kelvin wave is captured correctly.

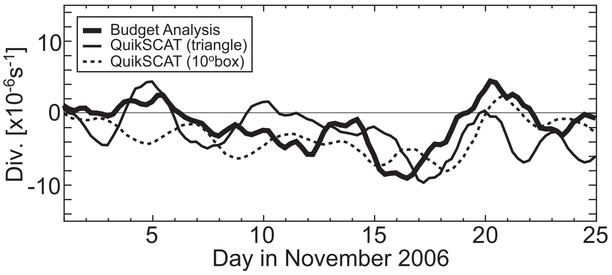

FIG. 5. Temporal variation of surface divergence, obtained by the budget analyses (thick) and QuikSCAT. The QuikSCAT data are areal averaged within the MISMO array triangle (thin solid) and 10° × 10° box centered at (0°, 75°E) (thin broken), respectively. All values are temporally averaged with a 2-day running mean filter.

Around the passage of the heat source (days 43–46), the Rossby wave component shows erroneous convergence (negative divergence), while the erroneous (positive) divergence is evident in the inertia–gravity wave component. After the passage of the heat source (day 47 and later), erroneous (positive) divergence is evident primarily in the Rossby wave components and secondarily in the inertia–gravity wave components.

To compare the result from the simulation to the actual values obtained in MISMO, the surface divergence from the budget analysis and Quick Scatterometer (QuikSCAT) observations (calculated from the wind data provided by Remote Sensing Systems; http://www.remss.com) are shown in Fig. 5. The divergence from the QuikSCAT is calculated for two regions: an area exactly covering the MISMO domain and a 10° box centered at (0°, 75°E) to reduce the effects of low temporal sampling and narrow spatial coverage (see Fig. 1 for these domains). Figure 5 indicates that from 15 to 17 November, when the budget-derived rainfall is larger than the other estimates (Fig. 3), the budget analysis shows excessive surface convergence (negative divergence) compared with that from the QuikSCAT winds. In contrast, on the following days (18–20 November) when the budget-derived rainfall is smaller than other estimates, surface (positive) divergence

---

[1] A similar result to the later method is achieved by sampling the model winds at the three MISMO sounding points and using line integrals to compute divergence.

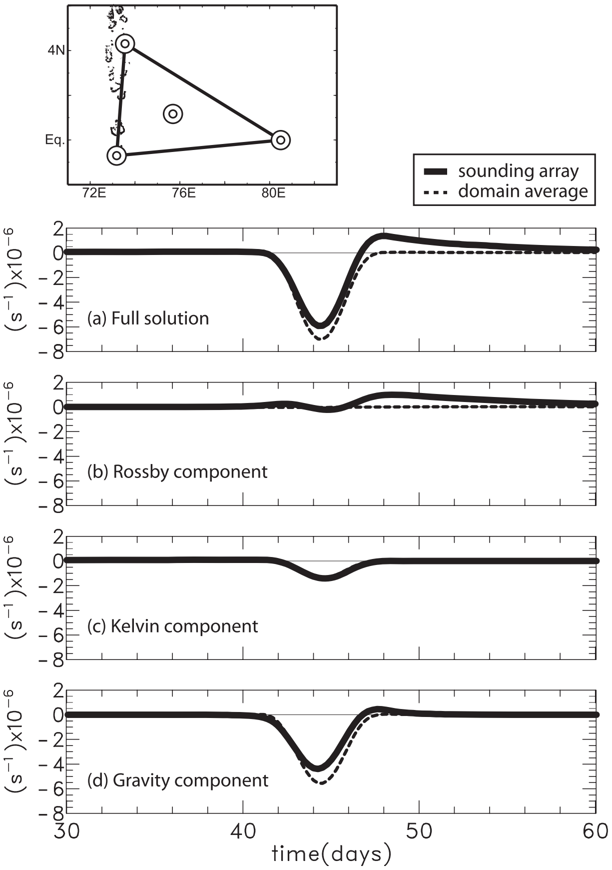

FIG. 6. As in Fig. 4, but with an additional point in the middle of the MISMO triangular array, as shown in top panel.

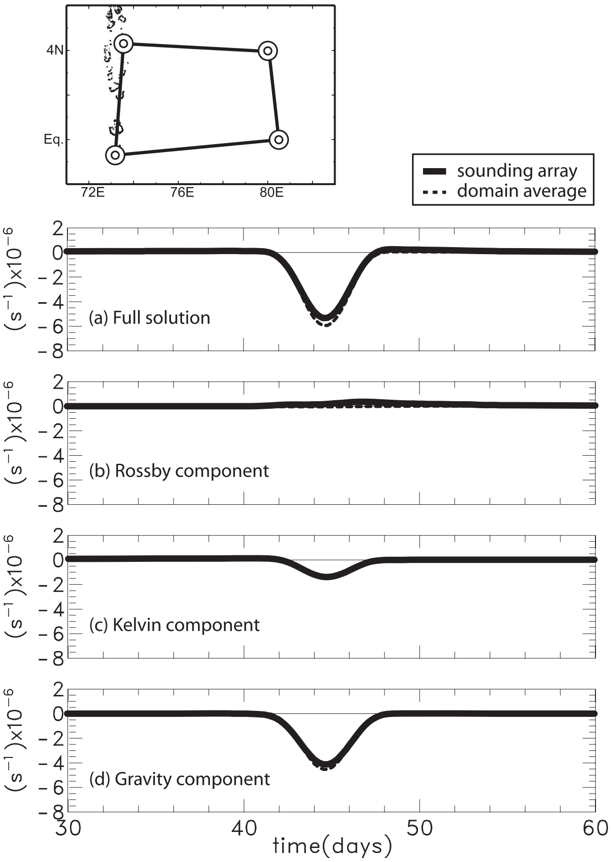

FIG. 7. As in Fig. 4, but for the rectangular sounding array by adding one point to the northwest of the MISMO triangular array as in the top panel.

from the budget analyses is persistently larger than that from the QuikSCAT winds. These erroneous low-level divergences resemble the results of the simulation in Fig. 4b, and suggest that the poorly sampled Rossby wave component results in erroneous budget-derived rainfall during the active phase. In addition, the excessive (positive) divergence in the inertia–gravity wave component appears to contribute to the underestimation in the budget-derived rainfall.

To further investigate the cause of this poor sampling, two additional experiments are performed by adding one virtual sounding site. The first experiment locates the additional point in the middle (centroid) of the MISMO triangle array (1.17°N, 75.73°E) to improve the distance between the sites without changing the shape of the array. The second experiment locates an additional virtual site to the northeast of the triangle (4.0°N, 80.0°E) to modify the shape of the array from the original triangle to a rectangle without dramatically changing the distance between sites.

Figures 6 and 7 show the results of these additional experiments. The experiment with the additional midpoint (Fig. 6) yields a similar result to the triangle configuration without a midpoint (Fig. 4), showing large erroneous divergence during and after the passage of the heat source. On the other hand, the experiment with the rectangular array (Fig. 7) acts to reduce the erroneous divergence from Rossby wave and inertia–gravity wave components, and thus, in the total divergence. These two simulations demonstrate that the rectangular form of the array is much better than the triangular form at capturing the divergence signature associated with an MJO-like circulation feature in a linear model.

5. Simulation using high-resolution, nonhydrostatic model output

The experiments in the previous section investigate the effects of a wind field from the idealized linear model. The actual atmosphere, on the other hand, contains nonlinear perturbations such as convection. To examine how different sounding arrays capture the atmosphere state to estimate Q_1 and Q_2 in a more realistic setting, we carried out experiments using the output from a high-resolution, nonhydrostatic cloud-resolving model.

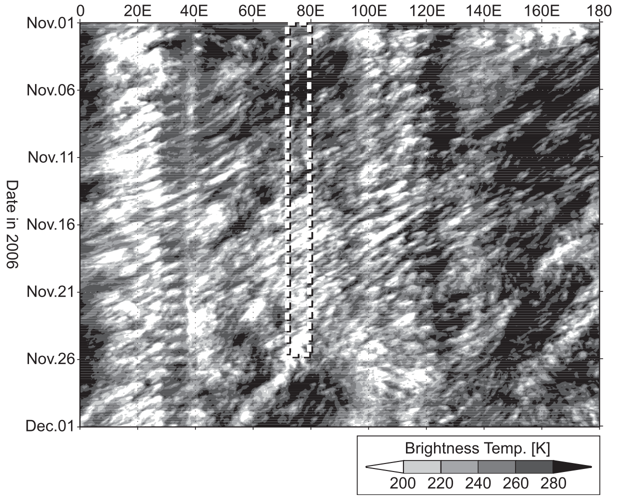

FIG. 8. Hovmöller diagram of the infrared brightness temperature reproduced from the NICAM output. The white broken box indicates the location and period of the MISMO sounding array during ASP.

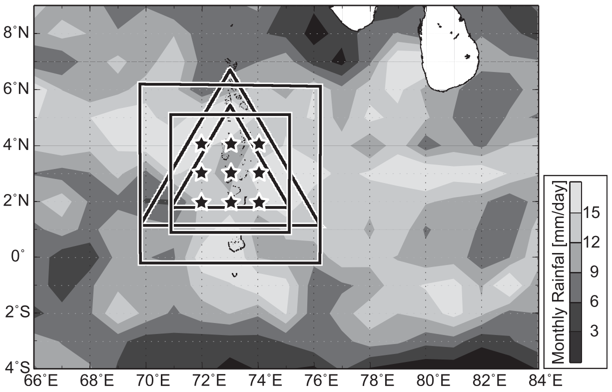

FIG. 9. The location and shape of four virtual sounding arrays used to simulate budget analyses with NICAM output, on the map of the rainfall averaged through the 30-day period. Each virtual array, displayed by equilateral triangles and squares, indicates the state without rotations used in the simulations. The stars are nine center positions of the virtual arrays used in the simulations.

The present study utilized output from the Nonhydrostatic Icosahedral Atmosphere Model (NICAM; Satoh et al. 2008). The experimental setting is the same as in Miura et al. (2009), which covers the MISMO-ASP. The advantages of using NICAM are 1) the NICAM reproduced the eastward-migrating cloud envelope similar to that observed in MISMO (Miura et al. 2009), and 2) the effect of cloud systems, which directly affect Q_1 and Q_2, is simulated without convective parameterization. Though the present study only utilized the result with horizontal grid spacing of about 14 km, the simulation reproduced well the eastward-propagating cloud envelope, which resembles the one observed in MISMO, as shown in the Hovmöller diagram of the simulated outgoing longwave radiation (OLR) (Fig. 8) and in Figs. 1–3 of Miura et al. (2009). The time interval of the NICAM output is 6 hourly, which is same as the budget analyses for the actual MISMO case described in section 2.

Using the NICAM output, sampling errors in the budget analyses are simulated as follows. First, we prepare two datasets each with 1° grid. One is "reconstructed" in the same manner used to compute budget analyses from the observed sounding, except using the vertical profiles of the NICAM output (i.e., winds and thermodynamic fields) at the virtual sounding sites. The other ("simulated") field is created by averaging the high-resolution NICAM output onto the 1° grid as "truth." Next, these two 1° grid datasets are used to compute gridded budgets that are averaged over the virtual arrays to create "reconstructed" and "simulated" fields, respectively. Comparing the budgets computed from the "simulated" and "reconstructed" gridded datasets provides a measure of the error in the budget analyses induced only by the difference of the sampling, that is, sampling of the virtual sounding arrays.

Four types of the virtual sounding arrays are constructed. As in Fig. 9, all virtual arrays are regular polygons, to simplify interpretation of the results. Two of the virtual arrays are squares to represent rectangular arrays and the other two are equilateral triangles representing triangular arrays. The larger triangle and smaller square are designed to have the same area as the MISMO sounding array. The side distances are set the same between the larger square and larger triangle, and between the smaller triangle and smaller square, such that the results can be interpreted independent of station spacing.

To examine the differences among the various arrays, ensemble averages are created for each virtual array; this suppresses the effects of random sampling error, including occasional sampling of extreme values. An ensemble dataset for each virtual array is created by centering the array at multiple locations with several rotation angles. The center locations consist of nine points including (3°N, 73°E) and eight surrounding points at 1° intervals, as shown by the stars in Fig. 9. The positions are selected to cover the area with large monthly averaged rainfall where large Q_1 and Q_2 values (and their perturbations) are expected. The rotation of the arrays is made in 10° increments, from 0° to 80° for squares and 0° to 110° for triangles. Thus the total number of perturbations for one virtual array is 9720 for the squares (9 center positions × 9 rotation angles × 4 times per day × 30 days) and 12 960 for the triangles (9 center positions × 12 rotation angles × 4 times per day × 30 days).

First, for the various virtual arrays, we show in Fig. 10 the averaged vertical profiles of "simulated" Q_1 and Q_2, which are considered here as "truth." The positive peak

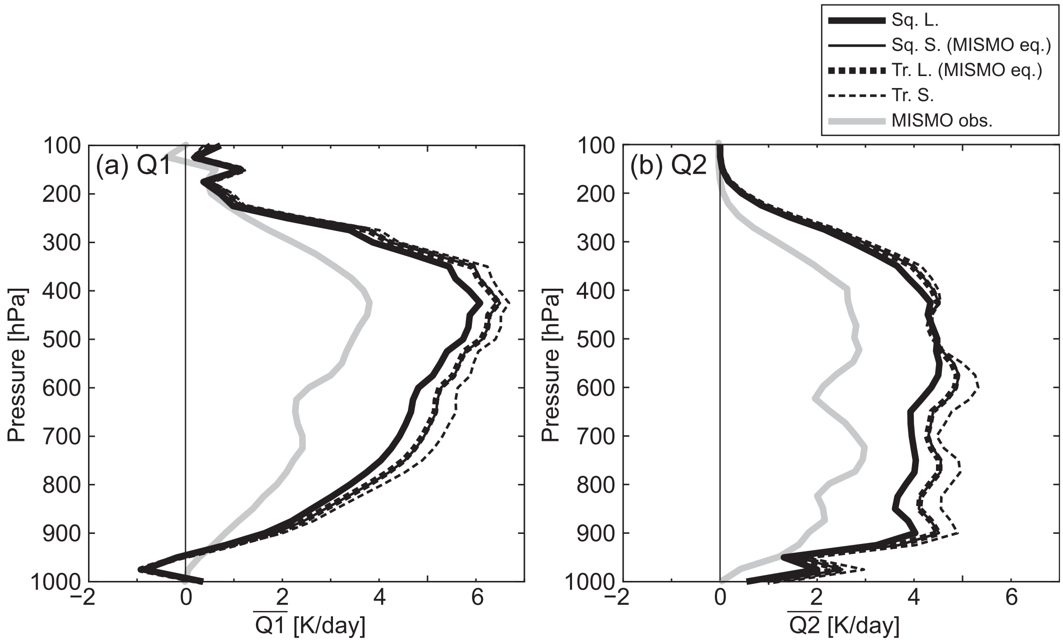

FIG. 10. Vertical profiles of the "simulated" Q_1 and Q_2, averaged within each virtual array. The legends are shortened as "Sq.L" for large square, "Sq.S" for small square (equivalent area to MISMO array), "Tr.L" for large triangle (equivalent area to MISMO array), and "Tr.S" for small triangle. The gray lines are observed Q_1 and Q_2, as in Fig. 2.

of Q_1 is at about 400 hPa, while Q_2 shows a flat peak from 400 to 900 hPa. These vertical structures are similar to those observed in MISMO, indicating that the Q_1 and Q_2 profiles during MISMO-ASP are reproduced well in the NICAM output.

On the other hand, the results from the various arrays differ about 1 K or less at all height levels both for Q_1 and Q_2. Especially, the difference between the small square and the large triangle is not significant even with the large number of samples. This indicates that the differences in the domain shape have no significant impact on the Q_1 and Q_2 profiles, at least in a temporal average sense for the 30-day period.

The differences between 30-day averaged "reconstructed" and "simulated" Q_1 and Q_2 profiles (hereinafter dQ_1 and dQ_2, respectively) are shown in Fig. 11 to investigate the averaged bias error of the reconstructed Q_1 and Q_2. In this figure, the dQ_1 and dQ_2 are smaller in the square arrays (solid lines) than in the triangular arrays (broken lines). In addition, the differences are smaller in the smaller arrays (thin lines) than in the larger arrays (thick lines). As a result, the differences are similar in the large square and the smaller triangle in the upper half of the troposphere. However in the lower troposphere, the larger square has smaller differences than the triangles.

To explore the relationship of the error on the budget analyses to other kinematic fields, Fig. 12 shows its time series along with several relevant parameters with dQ_1. The plot of vertically integrated dQ_1 (hereinafter $\langle dQ_1 \rangle$, where $\langle\ \rangle$ denotes the vertical average through the troposphere, i.e., from the surface to 100 hPa) shows a tendency similar to Fig. 11, in which the smaller and square arrays exhibit smaller differences. A detailed inspection of Fig. 12 reveals that the variability of $\langle dQ_1 \rangle$ increases dramatically after 22 November (denoted at period P3) with largest values on 26 November, even though the peak values of Q_1 are quite similar in both P2 and P3. These variations are highlighted by examining $[\langle dQ_1 \rangle / \langle Q_1 \rangle]$ in Fig. 12b, which is considerably larger during much of P3 than in P2. In other words, the error in the reconstructed field is much larger in P3 than in P2, with larger errors in the triangular arrays in the later period.

The corresponding time series of kinematic parameters in the lower troposphere are shown in Fig. 12c. The vorticity is relatively small in P2, followed by large fluctuations during P3. The relationship between the variation of vorticity and that of $\langle dQ_1 \rangle / \langle Q_1 \rangle$, especially in the triangular arrays, corresponds well to the results using the linear model in the previous section. Note that the main difference in vorticity between these periods is related primarily to the $\partial v/\partial x$ component. This suggests that a well-organized synoptic-scale vortex passed over the area of interest during P3, while only meridional shear producing weak vorticity was present in P2.

The variation of the equatorial zonal wind is also indicated by the zonal divergence ($\partial u/\partial x$) around the equator

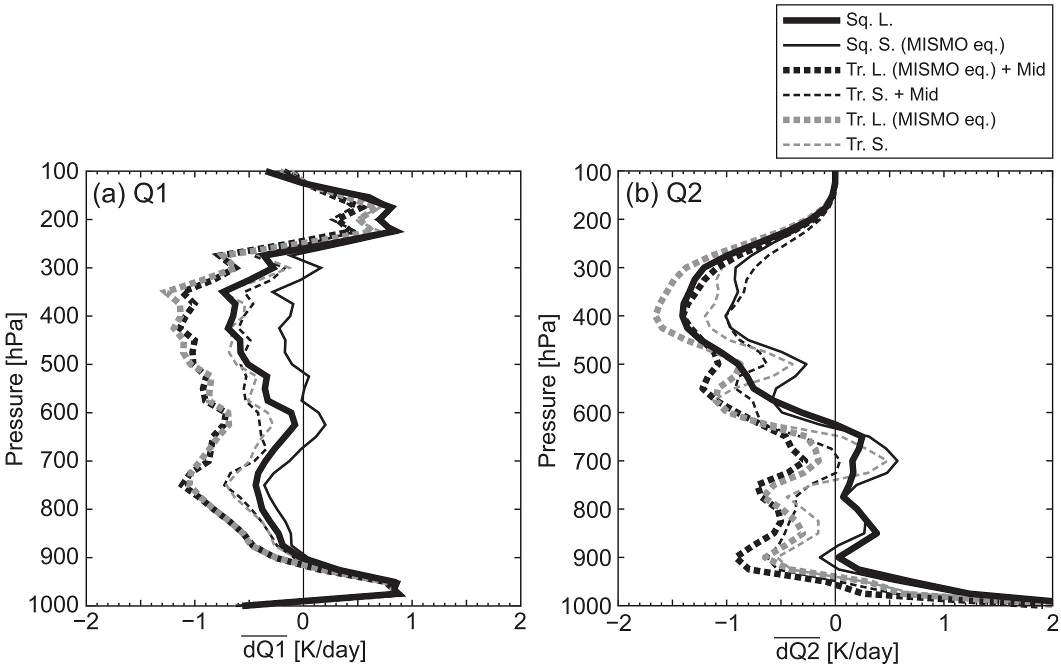

FIG. 11. Vertical profiles of the difference between "simulated" and "reconstructed" Q_1 and Q_2, averaged within each virtual array. Positive indicates that "simulated" value is larger. The key is as in Fig. 10, except that "+ mid" indicates additional midpoint in the virtual array.

in Fig. 12c, in which zonal convergence is significant in P2, becoming strongly divergent in P3. Thus, the temporal variation of the kinematic field changes from a period with zonal convergence at the equator without significant vorticity in P2 to a period with zonal divergence at the equator and large vorticity during P3. These temporal changes are similar to the kinematic field changes shown in Schubert and Masarik (2006) and in the previous section. That is, the Kelvin wave response, characterized by the zonal convergence, precedes the Rossby wave response with large vorticity as the MJO-like heat source moves eastward along the equator. Regarding the kinematic fields in P2 as a Kelvin wave signature, the smaller $\langle dQ_1\rangle/\langle Q_1\rangle$ in P2 than in P3 is consistent with the results in the previous section in which the Kelvin wave was well captured even by the MISMO array, that is, triangle array. On the other hand, the errors in the triangular arrays are generally larger than those of the rectangular arrays, even in P2 without significant vorticity. This suggests that rectangular sounding arrays are better suited at capturing the disturbances, including nonlinear perturbations.

Finally, it is interesting to note in Fig. 12 that the Q_1 error (i.e., $\langle dQ_1\rangle/\langle Q_1\rangle$) in the NICAM simulations has its negative maximum peak somewhat later than the peaks of maximum $\langle Q_1\rangle$ and vorticity. This resembles the pattern in the observed case (Fig. 3) in which the budget analyses based on the MISMO array resulted in significantly less rainfall in the latter half of the most active period from 15 to 21 November. This implies that the divergent errors generated by the rotational wind tend to be significant in the latter stage of the convectively active days with the temporal scale of a few to several days.

6. Discussion

The results of the simulations using the linear model and NICAM reveal that a simulated synoptic-scale wave disturbance in the convectively active phase adversely affected the accuracy of divergence computed from a triangular array similar to that used in MISMO. This section discusses how the actual case observed during the MISMO-ASP could be related to these simulations.

a. Active period

The largest discrepancies in budget-estimated rainfall during the MISMO-ASP occurred during the period of maximum rainfall, that is, around the core of the convectively active phase. In this period, there are several plausible sources to evoke the erroneous divergence associated with the triangular sounding array.

First is the Rossby response to the principle heat source as in Matsuno (1966). Considering the eastward movement of the convectively active area, it is reasonable to expect that the Rossby response followed the passage of the convectively active area, as in the simulation in section 4. The temporal variation of the budget-derived surface

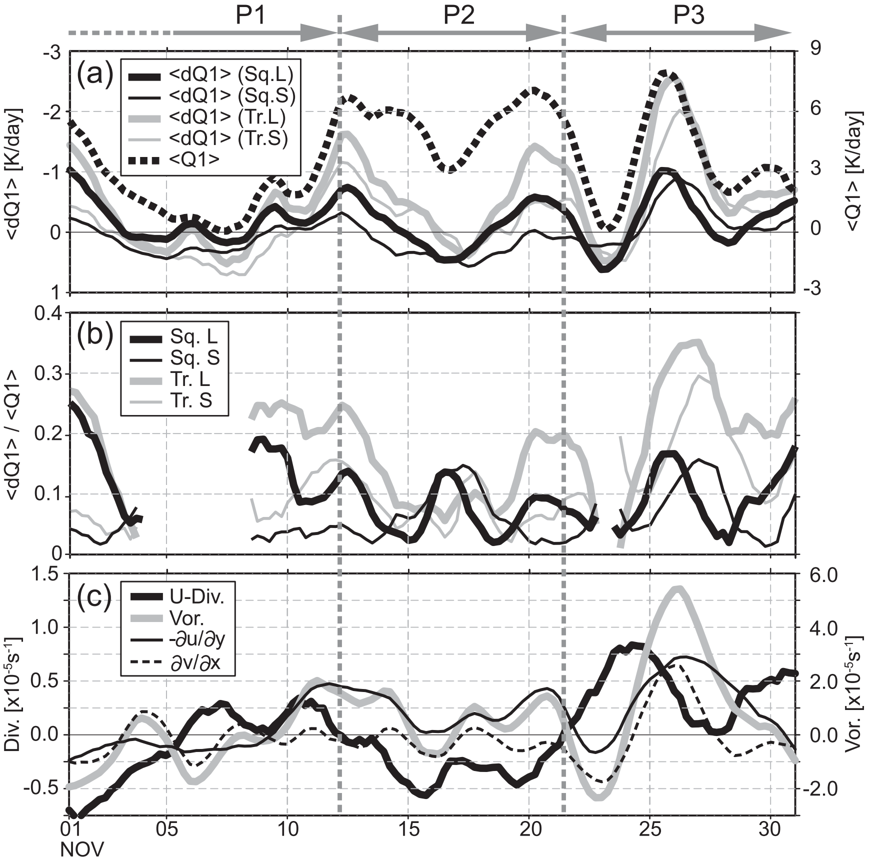

FIG. 12. Time series of parameters derived from NICAM simulations. (a) The vertically and areal-averaged Q_1 within small square and dQ$_1$ for various virtual arrays. (b) Absolute value of the ratio of $\langle dQ_1 \rangle$ to $\langle Q_1 \rangle$, not shown at times when $\langle Q_1 \rangle$ is less than 2 K. (c) Kinematic parameters at 850-hPa height, averaged for 6° × 6° domain. Zonal divergence (U-Div.) is for domain centered at (0°, 73°E), while the others are for domain centered at (3°N, 73°E). All parameters are filtered with a 2-day running mean, followed by a 1-day running mean for additional smoothing. The key abbreviations in (a) and (b) are as in Fig. 10. See text for periods designated P1, P2, and P3, which are separated by the vertical broken lines.

divergence and rainfall (see Table 1 and Fig. 3), in which the erroneously large rainfall amount with excessive convergence (negative divergence) from 15 to 17 November and following erroneously small rainfall amount with excessive (positive) divergence from 18 to 20 November, corresponds well to the simulated results in section 4. The NICAM simulation, which reproduced the eastward-migrating convective packet as observed in MISMO, also indicates a similar temporal variation (Fig. 12) in which zonal convergence precedes large synoptic-scale vorticity changes.

Regarding the Rossby response, such a circulation could be the result of a Rossby wave propagating from a remote region. The mode analyses using the method of Wheeler and Weickmann (2001; Fig. 5 of Y08) indicates that an $n = 1$ Rossby wave propagated from the Pacific and reached the sounding array at the beginning of the active period. This could be a second source for the error.

A third possible source for the error is the repeated passage of shorter and faster signals. The Hovmöller diagrams of the satellite infrared image and two surface radars (Fig. 13), or the GSMaP precipitation (not shown), indicate that fast westward-propagating signals passed over the MISMO domain repeatedly during the active phase with a period of about 2 days and the speed of about 18 m s^{-1} westward. This period and movement are similar to those of westward-propagating inertia–gravity waves (Takayabu 1994; Haertel and Kiladis 2004). A snapshot of one such disturbance is shown in Fig. 14 where a circular wind pattern in the Northern Hemisphere [around (4°N, 80°E) with the diameter of about one thousand kilometers] can be seen. The horizontal scale is similar to the simulated inertia–gravity wave in the linear model of Schubert and Masarik (2006), which causes error in estimating divergence by the MISMO sounding array (Fig. 4d).

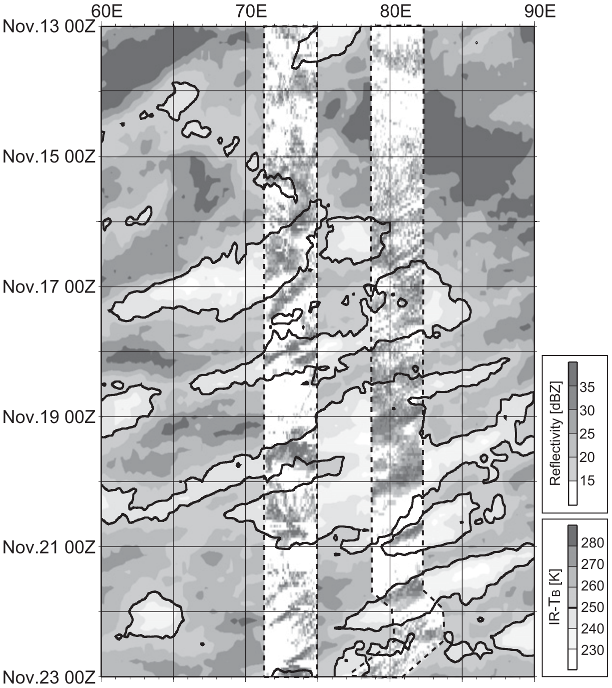

FIG. 13. Hovmöller diagram of the observed infrared brightness temperature averaged between 2°S and 2°N. The radar reflectivity (within 200 km in range distance), observed by the surface radars at Gan Island and at R/V *Mirai*, is overlaid in the area framed by the broken lines. The solid contour indicates the 250-K infrared brightness temperature. The radar reflectivity is quality controlled as in Katsumata et al. (2008).

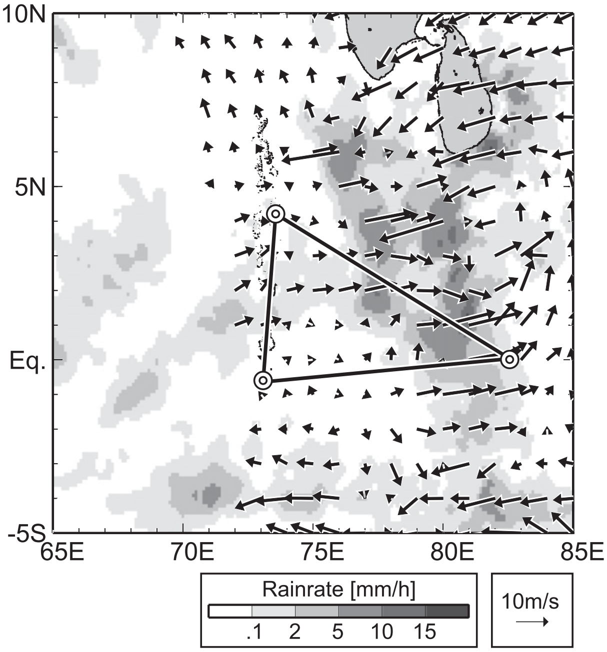

FIG. 14. Surface wind vector, observed by QuikSCAT, and rainfall rate (shaded) from GSMaP, at around 0000 UTC 20 Nov. The MISMO sounding array is also shown by the triangle with double circles.

In the simulation, the erroneous divergence by the inertia–gravity wave is positive for most of the period. In Fig. 13, one can see that the westward-propagating cloud signal over the sounding array (between two radar sites) becomes apparent after 18 November. This temporal variation corresponds well to that of the erroneous divergence (Fig. 3) that turns to positive after 18 November, resulting in the erroneously small budget-derived rainfall (Fig. 2).

With regards to the fast speed of the inertia–gravity waves, their sampling by the MISMO network should also be considered. The propagation speed (about 18 m s^{-1}) of the disturbances enables them to pass over the sounding array (about 800 km in zonal width) in about 12 h. Considering that their zonal scale was comparable in size to the sounding array, the MISMO network would have only sampled a few snapshots of each disturbance packet. In addition, the soundings at Hulhule (4.2°N, 73.5°E) were every 12 h before 20 November. These factors suggest that such fast-propagating disturbance in the active phase would have been undersampled by the MISMO sounding array.

The above discussion qualitatively reveals the contribution of these three wave sources, described above, to the erroneous divergence in the active phase during MISMO. The quantitative evaluation of each effect is, however, left for future studies.

b. Preactive period

In contrast to the active period, good agreement among the various rainfall estimates is found in the period prior to the convectively active period in the observed MISMO-ASP (Fig. 3). As shown in KJC09, this period is characterized by the repeated passage of the eastward-propagating Kelvin wave–like disturbances. The simulation using NICAM output (in section 5) shows the same tendency in the former half of the convectively active period (P2), with relatively little error in estimated Q_1 even using the triangular arrays, and with the zonal convergence at the equator resembling a Kelvin wave–type wind field. These results, both from the observations and NICAM output, could be understood by the linear model simulation (section 4) in which the divergence from the Kelvin wave component of the flow is well resolved by the MISMO triangular array.

Next, we consider the sampling of the Kelvin-like disturbances in the preactive period. During the period prior to the convectively active phase, the propagation speed of the Kelvin wave–like disturbances over the MISMO region was around 8 m s^{-1} (KJC09). Considering the zonal distance of the MISMO triangle array (about 800 km), the disturbance would persist within the sounding network for more than 24 h. Even with the 12-hourly observation of the radiosonde at Gan and Male in the preactive period (see section 2), the slower propagation speed would enable the sounding network to better sample the disturbance structure and capture its kinematic features. In addition, two of the sounding sites, Gan Island and R/V *Mirai*, were located quite close to the equator, where the amplitude of the Kelvin wave is theoretically largest. This distribution of sounding sites likely contributed to capturing the Kelvin wave–type disturbances more accurately. Thus it appears that the sounding array during MISMO was successful in capturing the disturbances which brought rainfall in the period prior to the convectively active phase.

c. *Effect of random sampling error*

Here we consider the impact of random sampling errors on the MISMO budgets, which was examined by Mapes et al. (2003) for previous experiments. To estimate how temporal wind variations affect errors in divergence, we utilize the wind profiler dataset from the R/V *Mirai* during MISMO-ASP (Kawano et al. 2009), which provides wind profiles every 10 min below 5-km height. We first calculate the difference between the instantaneous wind speed in the zonal and meridional components from the 6-h running mean to estimate how the instantaneous observed wind represents the temporal average. Since the root-mean-square (RMS) of the deviations for zonal and meridional component is nearly the same, we use the variation of the zonal component for all wind components at all three points in the MISMO array. With this assumption, the RMS deviation of divergence is calculated from the dataset of the zonal wind deviations using the line-integral method. The resulting divergence error is about $4 \times 10^{-6}\ \mathrm{s}^{-1}$ for instantaneous observations at every 6 h. This value could be halved by averaging four points as in Mapes et al. (2003). By applying a 2-day running mean (i.e., nine data points), which is used to examine the temporal variations in this study, the divergence error due to random sampling effects could be reduced to $1 \times 10^{-6}\ \mathrm{s}^{-1}$. This value is comparable to the simulated error of divergence in the linear model (Fig. 4), or the difference between divergences observed by QuikSCAT and estimated in the budget analyses (Fig. 5). It is suggested that the effects of undersampling synoptic-scale disturbances in MISMO become more apparent than random sampling errors by applying running mean filters of 2 days or longer.

7. Concluding remarks

This study investigates the reliability of the budget analyses in the *Mirai* Indian Ocean Cruise for the Study of the MJO Onset project for the 26-day period from 31 October to 25 November 2006 [MISMO arrayed sounding period (MISMO-ASP)] when a three sounding site array was deployed. To evaluate the reliability, the budget-derived rainfall is compared with the rainfall estimated from other sources (gauges, satellites). The ASP-averaged rainfall from the budget analyses compares well to the other estimates. While the temporal variations determined by the other estimates compare favorably to budget estimate before the convectively active phase (before 15 November), considerable differences are found in the subsequent convectively active phase.

To understand the poor performance of the budget estimates in the latter period, analyses from two model simulations are used. The first simulation is from a linear, equatorial β-plane model (Schubert and Masarik 2006), which is forced with an MJO-like heating. The second simulation is from the high-resolution AGCM named ‘‘NICAM’’ (Satoh et al. 2008), which reproduced the convectively active phase in MISMO-ASP (Miura et al. 2009).

Both simulations indicate that the error in the budget analyses using a triangular sounding array arises in the convectively active period when the rotational components of the winds are large. Possible sources to invoke the error include a Rossby wave response from the principle heat source, a Rossby wave that propagates in from the Pacific, and high-frequency westward-propagating disturbances like the inertia–gravity wave. In contrast, the simulations also indicate that error in the budget analyses is small in the former period when a Kelvin wave–type wind pattern is present, that is, zonal convergence dominates the low-level wind field.

In addition, the simulations also indicate that a rectangular-type sounding array can better capture circulations with rotational wind patterns. Furthermore, the NICAM simulation showed that the budget error with the rectangular array is suppressed by one-third of that with the triangular array even in the period without significant rotational winds. On the other hand, a more detailed study is needed to help us better understand the precise reasons why the rectangular array provides a better estimation of divergence than the triangular array.

The results of this present study suggest that the MISMO sounding array was not optimal for capturing the full range of equatorial circulations, though it did successfully sample the disturbances in the period leading up to the convectively active phase investigated in KJC09. While these results lend confidence to the study of KJC09, the reliability of the temporal variations of the budgets in the convectively active phase of MISMO remains low.

The convectively active phase of intraseasonal variations, including the MJO, consists of complex circulations over a wide spectrum of time and space scales (Kiladis et al. 2009). Recent studies have shown that the convectively active phase of the intraseasonal oscillation (including the MJO) consists of the convectively coupled waves (e.g., Masunaga et al. 2006; Roundy and Frank 2004). Accurate estimates of the diabatic heating with high temporal resolution are crucial to investigate the nature of these convectively coupled waves. To achieve this goal in future field campaigns, a more enhanced sounding array than MISMO is required, namely one with four or more sounding sites.

Acknowledgments. The authors acknowledge Dr. W. H. Schubert, Mr. M. Masarik, and Mr. B. McNoldy for their suggestions and help in providing the linear model numerical simulations. All participants in MISMO observations are acknowledged for their skillful efforts to obtain and provide the observational dataset. The comments from three anonymous reviewers were helpful in improving the manuscript. Special thanks are given to Dr. M. Satoh and Dr. H. Miura for providing the NICAM dataset. The NICAM simulations were carried out using the Earth Simulator and were supported by the program of CREST/JST. The SSM/I and QuikSCAT datasets are obtained from the Remote Sensing Systems Co. (http://www.remss.com). Part of this research has been supported by the JEPP-HARIMAU project. Richard Johnson and Paul Ciesielski were supported under NASA Grant NNX07AD35G.

REFERENCES

Ciesielski, P. E., W. H. Schubert, and R. H. Johnson, 1999: Large-scale heat and moisture budgets over the ASTEX region. *J. Atmos. Sci.,* **56,** 3241–3261.

——, R. H. Johnson, P. T. Haertel, and J. Wang, 2003: Corrected TOGA COARE sounding humidity data: Impact on diagnosed properties of convection and climate over the warm pool. *J. Climate,* **16,** 2370–2384.

Haertel, P. T., and G. N. Kiladis, 2004: Dynamics of 2-day equatorial waves. *J. Atmos. Sci.,* **61,** 2707–2721.

Hartmann, D. L., H. H. Hendon, and R. A. Houze Jr., 1984: Some implications of the mesoscale circulations in tropical cloud clusters for large-scale dynamics and climate. *J. Atmos. Sci.,* **41,** 113–121.

Johnson, R. H., and P. E. Ciesielski, 2000: Rainfall and radiative heating rates from TOGA COARE atmospheric budgets. *J. Atmos. Sci.,* **57,** 1497–1514.

——, and ——, 2002: Characteristics of the 1998 summer monsoon onset over the northern South China Sea. *J. Meteor. Soc. Japan,* **80,** 561–578.

Katsumata, M., T. Ushiyama, K. Yoneyama, and Y. Fujiyoshi, 2008: Combined use of TRMM/PR and disdrometer data to correct reflectivity of ground-based radars. *SOLA,* **4,** 101–104, doi:10.2151/sola.2008-026.

——, R. H. Johnson, and P. E. Ciesielski, 2009: Observed synoptic-scale variability during the developing phase of an ISO over the Indian Ocean during MISMO. *J. Atmos. Sci.,* **66,** 3434–3448.

Kawano, N., H. Hashiguchi, K. Yoneyama, and S. Fukao, 2009: Lower atmosphere observations over the equatorial Indian Ocean with a shipborne lower troposphere radar during MISMO field experiment. *Radio Sci.,* **44,** RS6011, doi:10.1029/2008RS003885.

Kiladis, G. N., M. C. Wheeler, P. T. Haertel, K. H. Straub, and P. E. Roundy, 2009: Convectively coupled equatorial waves. *Rev. Geophys.,* **47,** RG2003, doi:10.1029/2008RG000266.

Kubota, T., and Coauthors, 2007: Global precipitation map using satellite-borne microwave radiometers by the GSMaP Project: Production and validation. *IEEE Trans. Geosci. Remote Sens.,* **45,** 2259–2275.

Lin, J., B. Mapes, M. Zhang, and M. Newman, 2004: Stratiform precipitation, vertical heating profiles, and the Madden–Julian oscillation. *J. Atmos. Sci.,* **61,** 296–309.

Mapes, B. E., and R. A. Houze Jr., 1995: Diabatic divergence profiles in western Pacific mesoscale convective systems. *J. Atmos. Sci.,* **52,** 1807–1828.

——, P. E. Ciesielski, and R. H. Johnson, 2003: Sampling errors in rawinsonde-array budgets. *J. Atmos. Sci.,* **60,** 2697–2714.

Masunaga, H., T. S. L'Ecuyer, and C. D. Kummerow, 2006: The Madden–Julian oscillation recorded in early observations from the Tropical Rainfall Measurement Mission (TRMM). *J. Atmos. Sci.,* **63,** 2777–2794.

Matsuno, T., 1966: Quasi-geostrophic motions in the equatorial area. *J. Meteor. Soc. Japan,* **44,** 25–43.

Miura, H., M. Satoh, and M. Katsumata, 2009: Spontaneous onset of a Madden–Julian oscillation event in a cloud-system-resolving simulation. *Geophys. Res. Lett.,* **36,** L13802, doi:10.1029/2009GL039056.

Nicholls, M. E., R. A. Pielke, and W. R. Cotton, 1991: Thermally forced gravity waves in an atmosphere at rest. *J. Atmos. Sci.,* **48,** 1869–1884.

Nuss, W. A., and D. W. Titley, 1994: Use of multiquadric interpolation for meteorological objective analysis. *Mon. Wea. Rev.,* **122,** 1611–1631.

O'Brien, J. J., 1970: Alternative solutions to the classical vertical velocity problem. *J. Appl. Meteor.,* **9,** 198–203.

Roundy, P. E., and W. M. Frank, 2004: Effects of low-frequency wave interactions on intraseasonal oscillations. *J. Atmos. Sci.,* **61,** 3025–3040.

Satoh, M., T. Matsuno, H. Tomita, H. Miura, T. Nasuno, and S. Iga, 2008: Nonhydrostatic Icosahedral Atmospheric Model (NICAM) for global cloud resolving simulations. *J. Comput. Phys.,* **227,** 3486–3514.

Schubert, W. H., and M. T. Masarik, 2006: Potential vorticity aspects of the MJO. *Dyn. Atmos. Oceans,* **42,** 127–151.

Schumacher, C., R. A. Houze Jr., and I. Kraucunas, 2004: The tropical dynamical response to latent heating estimates derived from the TRMM precipitation radar. *J. Atmos. Sci.,* **61,** 1341–1358.

——, P. E. Ciesielski, and M. H. Zhang, 2008: Tropical cloud heating profiles: Analyses from KWAJEX. *Mon. Wea. Rev.,* **136,** 4289–4300.

Takahashi, S., F. Kondo, O. Tsukamoto, Y. Ito, S. Hirayama, and H. Ishida, 2005: On-board automated eddy flux measurement system over open ocean. *SOLA,* **1,** 37–40, doi:10.2151/sola.2005-011.

Takayabu, Y. N., 1994: Large-scale cloud disturbances associated with equatorial waves. Part II: Westward-propagating inertio-gravity waves. *J. Meteor. Soc. Japan,* **72,** 451–465.

Wentz, F. J., and R. W. Spencer, 1998: SSM/I rain retrievals within a unified all-weather ocean algorithm. *J. Atmos. Sci.,* **55,** 1613–1627.

Wheeler, M., and K. M. Weickmann, 2001: Real-time monitoring and prediction of modes of coherent synoptic to intraseasonal tropical variability. *Mon. Wea. Rev.,* **129,** 2677–2694.

Yanai, M., S. Esbensen, and J.-H. Chu, 1973: Determination of bulk properties of tropical cloud clusters from large-scale heat and moisture budgets. *J. Atmos. Sci.,* **30,** 611–627.

Yoneyama, K., M. Fujita, N. Sato, M. Fujiwara, Y. Inai, and F. Hasebe, 2008a: Correction for radiation dry bias found in RS92 radiosonde data during the MISMO field experiment. *SOLA,* **4,** 13–16.

——, and Coauthors, 2008b: MISMO field experiment in the equatorial Indian Ocean. *Bull. Amer. Meteor. Soc.,* **89,** 1889–1903.

Yu, L., X. Jin, and R. A. Weller, 2008: Multidecade global flux datasets from the Objectively Analyzed Air–Sea Fluxes (OAFlux) Project: Latent and sensible heat fluxes, ocean evaporation, and related surface meteorological variables. Woods Hole Oceanographic Institution OAFlux Project Tech. Rep. OA-2008-01, 64 pp.

Zhang, C., and S. Hagos, 2009: Bi-modal structure and variability of large-scale diabatic heating in the tropics. *J. Atmos. Sci.,* **66,** 3621–3640.

Zhang, M. H., J. L. Lin, R. T. Cederwall, J. J. Yio, and S. C. Xie, 2001: Objective analysis of the ARM IOP data: Method and sensitivity. *Mon. Wea. Rev.,* **129,** 295–311.